

Integrated AlGaInAs-silicon evanescent racetrack laser and photodetector

Alexander W. Fang¹, Richard Jones², Hyundai Park¹, Oded Cohen³, Omri Raday³, Mario J. Paniccia², & John E. Bowers¹

¹University of California, Santa Barbara, Department of Electrical and Computer Engineering, Santa Barbara, CA 93106, USA

²Intel Corporation, 2200 Mission College Blvd, SC12-326, Santa Clara, California 95054, USA

³Intel Corporation, S.B.I. Park Har Hotzvim, Jerusalem, 91031, Israel

awfang@ece.ucsb.edu

Abstract

Recently, AlGaInAs-silicon evanescent lasers have been demonstrated as a method of integrating active photonic devices on a silicon based platform. This hybrid waveguide architecture consists of III-V quantum wells bonded to silicon waveguides. The self aligned optical mode leads to a bonding process that is manufacturable in high volumes. Here we give an overview of a racetrack resonator laser integrated with two photo-detectors on the hybrid AlGaInAs-silicon evanescent device platform. Unlike previous demonstrations of hybrid AlGaInAs-silicon evanescent lasers, we demonstrate an on-chip racetrack resonator laser that does not rely on facet polishing and dicing in order to define the laser cavity. The laser runs continuous-wave (c.w.) at 1590 nm with a threshold of 175 mA, has a maximum total output power of 29 mW and a maximum operating temperature of 60 C. The output of this laser light is directly coupled into a pair of on chip hybrid AlGaInAs-silicon evanescent photodetectors used to measure the laser output.

Keywords: Silicon evanescent laser, Silicon photonics, integration, photodetector, semiconductor laser

1. Introduction

Silicon photonics has received a lot of attention by researchers with the hopes to leverage the low cost manufacturing infrastructure of CMOS photonics for applications such as chip to chip and board to board interconnects[1-4]. This work has been focused on the building blocks of photonic communication systems such as lasers [5-8], modulators, photodetectors, and others [9-15]. Our work has been focused on developing a hybrid integration platform that allows for III-V material functionality, such as light amplification and detection, to be utilized on silicon waveguide based devices. This platform consists of a III-V epitaxial structure bonded to a silicon waveguide to make a hybrid waveguide such that its optical mode lies primarily in the silicon region with a small portion of the mode overlapping the quantum wells of the III-V structure for optical gain. The optical mode characteristics are predominately defined by the silicon waveguide processing. Bonding can be performed without critical alignment. The remaining critical alignment steps, such as the definition of electrical current injection channels, utilize standard lithographic techniques leading to a high volume, low-cost, solution for active devices on silicon. The first hybrid laser demonstration relied on the dicing and polishing of straight hybrid waveguides to define a Fabry-Perot laser cavity [16]. Here we review a monolithic hybrid AlGaInAs-silicon evanescent laser based on a racetrack-resonator-topography. The laser runs continuous-wave (c.w.) with a threshold of 175 mA, a maximum total output power of 29 mW and maximum operating temperature of 60 °C. Moreover we report the integration of this laser with a hybrid AlGaInAs-silicon evanescent photodetector used to measure the laser output[17].

2. Device Structure and Design

The hybrid AlGaInAs-silicon evanescent device cross section is shown in figure 1. The devices are fabricated using an AlGaInAs quantum well epitaxial structure that is bonded to a low-loss silicon rib waveguide. The silicon rib waveguide is formed on the (100) surface of an undoped silicon-on-insulator (SOI) substrate with a 1 μm thick buried oxide using standard projection photolithography and Cl₂/Ar/HBr- based plasma reactive ion etching. The silicon waveguide was

fabricated with a final height, width, and rib-etch depth of 0.69 μm , 1.65 μm , and 0.5 μm , respectively. The III-V epitaxial structure is grown on an InP substrate and its details are shown in Table 1. The detailed fabrication procedure can be found in ref 18. The calculated overlap of the optical mode with the silicon waveguides is 64 % while there is a 4.2 % overlap in the quantum wells.

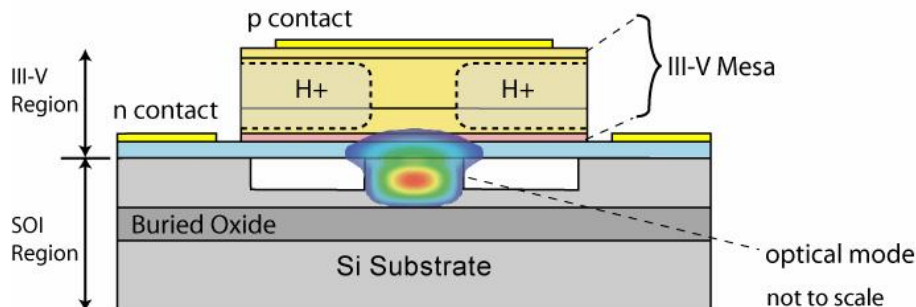


Fig. 1. The hybrid silicon-III-V device cross section structure.

This III-V structure is transferred to the patterned silicon wafer through a low temperature oxygen plasma assisted wafer bonding process [19]. The low temperature process consists of a thorough solvent cleaning procedure, followed by surface treatments with buffered HF for silicon and NH_4OH for InP, and an additional surface treatment in an oxygen plasma reactive ion etch chamber. The samples surfaces are then placed in physical contact at room temperature and subsequently annealed at 300 $^\circ\text{C}$ with an applied pressure of 1.5 MPa for 12 hours under vacuum.

III-V Epitaxial growth layer structure

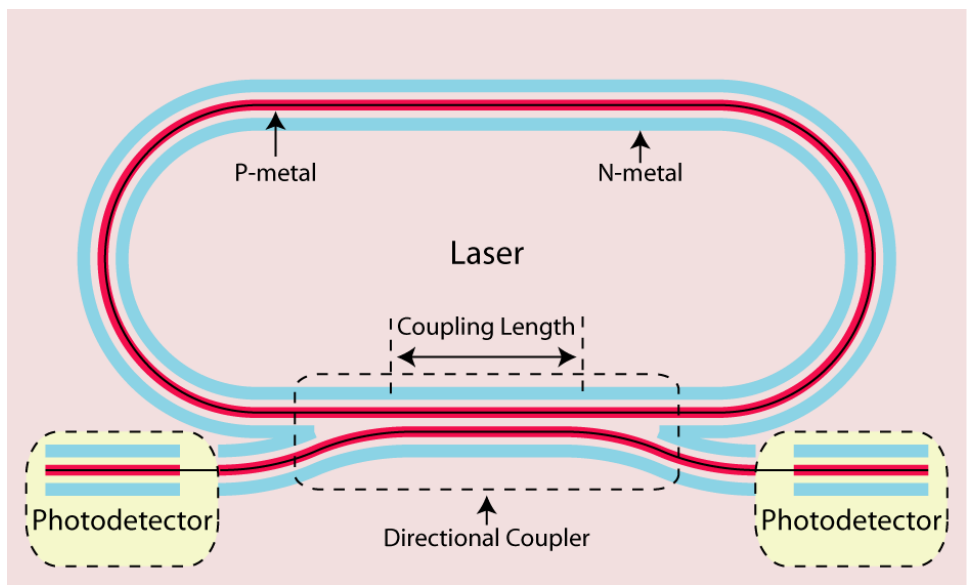
Name	Composition	Doping Concentration	Thickness
P contact layer	P-type $\text{In}_{0.53}\text{Ga}_{0.47}\text{As}$	$1 \times 10^{19} \text{ cm}^{-3}$	0.1 μm
Cladding	P-type InP	$1 \times 10^{18} \text{ cm}^{-3}$	1.5 μm
SCH	P-type $\text{Al}_{0.131}\text{Ga}_{0.34}\text{In}_{0.528}\text{As}$, 1.3 μm	$1 \times 10^{17} \text{ cm}^{-3}$	0.25 μm
Quantum Wells	$\text{Al}_{0.089}\text{Ga}_{0.461}\text{In}_{0.45}\text{As}$, 1.3 μm (9x)	undoped	10 nm
	$\text{Al}_{0.055}\text{Ga}_{0.292}\text{In}_{0.653}\text{As}$, 1.7 μm (8x)	undoped	7 nm
N layer	N-type InP	$1 \times 10^{18} \text{ cm}^{-3}$	110 nm
Super Lattice	N-type $\text{In}_{0.85}\text{Ga}_{0.15}\text{As}_{0.327}\text{P}_{0.673}$ (2x)	$1 \times 10^{18} \text{ cm}^{-3}$	7.5 nm
	N-type InP (2x)	$1 \times 10^{18} \text{ cm}^{-3}$	7.5 nm
N bonding layer	N-type InP	$1 \times 10^{18} \text{ cm}^{-3}$	10 nm

Table 1, III-V epitaxial grown layer structure

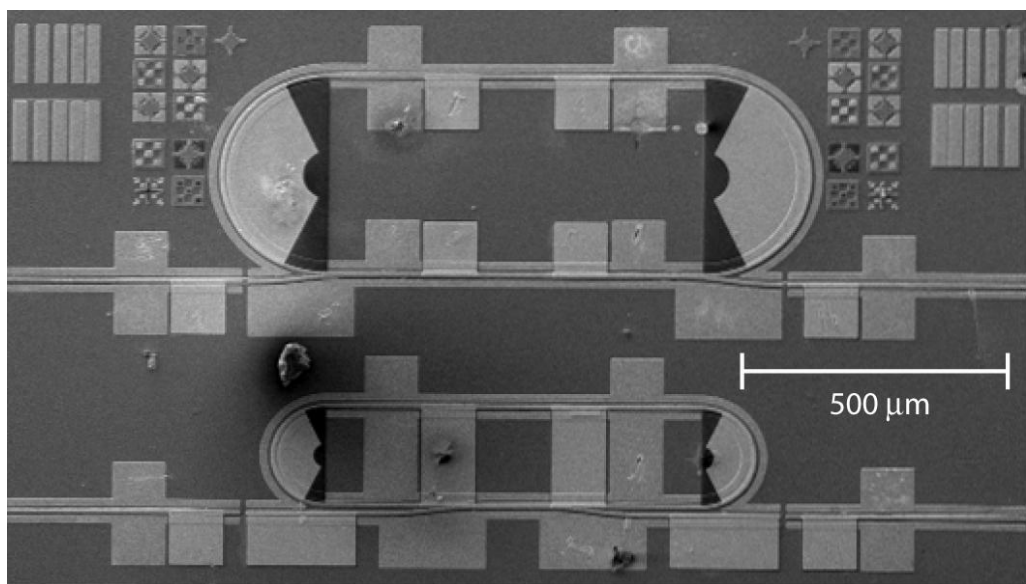
After InP substrate removal with a mixture of $\text{HCl}/\text{H}_2\text{O}$, 10 μm wide mesas are formed using photolithography and by $\text{CH}_4/\text{H}/\text{Ar}$ - based plasma reactive ion etching through the p-type layers and $\text{H}_3\text{PO}_4/\text{H}_2\text{O}_2$ selective wet etching of the quantum well layers to the n-type layers. Ni/AuGe/Ni/Au alloy n-contacts are deposited onto the exposed n-type InP layers on both sides of the mesa. 4 μm wide Pd/Ti/Pd/Au p-contacts are then deposited on the center of the mesas. The p-region on the two sides of the mesa are implanted with protons (H^+) which electrically insulates the p-type InP [20] resulting in a ~ 4 micron wide p-type current channel down through the non conductive p-type mesa, preventing lateral current spreading in the p-type mesa. The electrical current flows through the center of the mesa to achieve a large overlap with the optical mode. Ti/Au P-probe pads are deposited on the top of the mesas and on the sides of the mesa. A 0.5 μm thick SiN layer is used between the P-probe pad and the n contact for insulation.

The laser layout is shown in Figure 2. It consists of a racetrack ring resonator with a straight waveguide length of 700 microns. A directional coupler is formed on the bottom arm by placing a bus waveguide 0.5 micron away from the racetrack. Four device designs were fabricated with varying ring radius, and coupler interaction lengths ($L_{\text{interaction}}$). Table 2 shows the device layout breakdown with the corresponding cavity lengths (L_{cavity}) and the computed coupling percentage to the bus waveguide. The laser power is collected into the two 440 micron long photodetectors. These

photo-detectors have the same waveguide architecture as the hybrid laser, the only difference being that they are reverse biased to collect photo-generated carriers.



(a)



(b)

Fig. 2. a) The layout of the racetrack resonator and the photodetectors. b) A top view SEM micrograph of two racetrack resonator lasers. The racetrack resonator lasers on the top and bottom have radii of 200 and 100 microns, respectively

The additional losses due to waveguide bending as a function of radius were calculated using Beamprop (Figure 3). The $R = 200$ micron devices lie within the low bend loss region. $R = 100$ micron devices were fabricated since the available gain can still overcome the additional losses due to the bends.

Radius	L_{cavity}	$L_{\text{Interaction}}$	Computed Feedback Coupling
200 μm	2656 μm	600 μm	3 %
		400 μm	12.6%
100 μm	2028 μm	300 μm	36%
		100 μm	85%

Table 2, Ring dimensions and coupling parameters

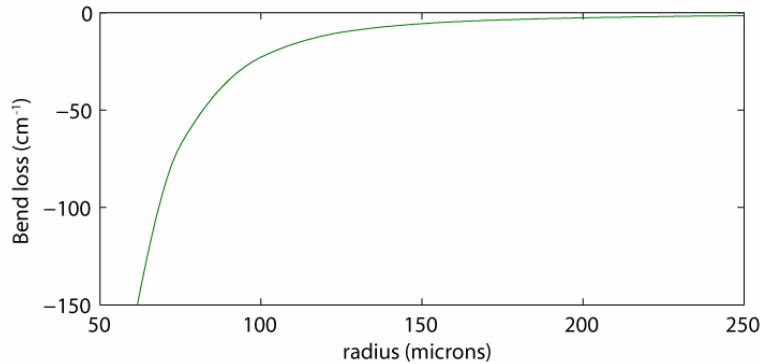


Fig 3. The simulated additional bend loss as a function of radius

3. Photodetector

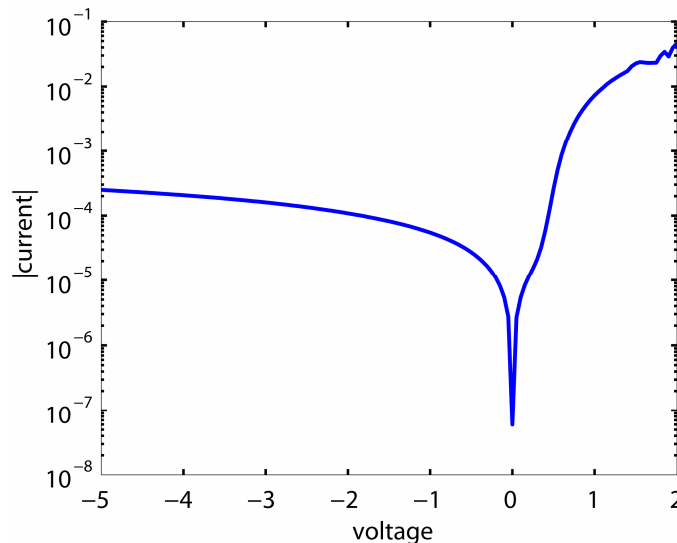


Fig 4. The IV characteristics of the Silicon evanescent photodetector

The responsivity of the photodetectors was measured by dicing and polishing a discrete detector in the same chip and launching a laser light into the detector through a lensed fiber. The fiber coupled responsivity was measured to be .25 A/W at 1580nm. Taking into consideration the $\sim 30\%$ reflection off the waveguide facet and an estimated $5.25 \pm .25$ dB coupling loss, we estimate the photodetector responsivity to be in the range of 1.25 - 1.11 A/W. This corresponds to a quantum efficiency between 97%-86%. We use a responsivity of 1.25 A/W in the remainder of this paper such that the laser power values are on the conservative side. The detector dark current was measured to be $\sim 250 \mu\text{A}$ (figure 4).

4. Racetrack Laser

The laser is driven by applying a positive bias voltage to the top p-probe contact while the optical power is measured by the two photodetectors on each side of the coupler. The photocurrent is measured while reverse biasing the photodetectors at -5V. Since the testing of the lasers are done all on chip without polishing and dicing, the lasing spectrum is measured by collecting scattered light near the bends of the ring through a fiber probe. The entire silicon chip is mounted on a TEC controller which allows the operating temperature of the laser to be varied from 0 °C to 80 °C.

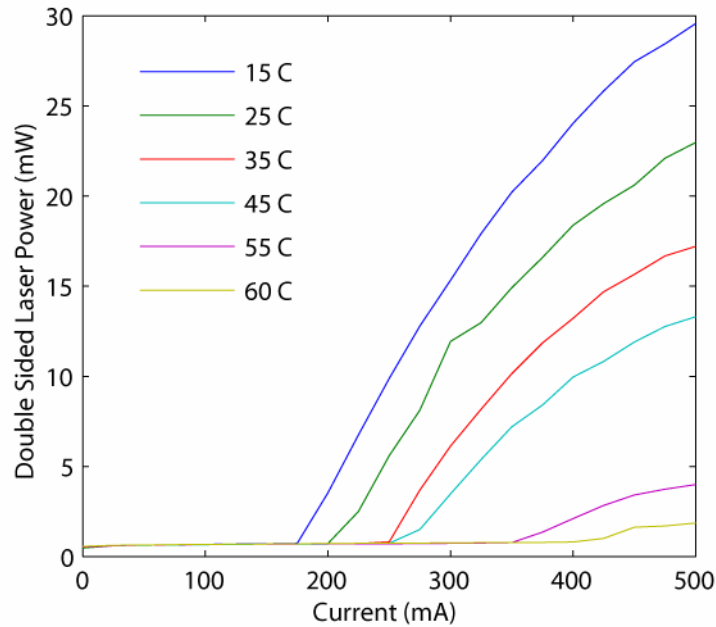


Fig. 5. The LI curve for a laser with radius $R = 200$ microns, and $L_{interaction} = 400$ microns for various temperatures

Figure 5 shows the measured total c.w. laser output power which is the sum of the optical power measured at both detectors as a function of injected current for various operating temperatures ranging from 15 to 60 °C for the laser with a ring radius and coupling interaction length of 200 microns and 400 microns respectively. As can be seen from Fig. 5, the laser threshold is 175 mA with a maximum output power of 29 mW at 15 °C. The maximum power is limited by the available drive current to the device. The laser has a 60 °C maximum lasing temperature with a characteristic temperature of 55 K. The laser has a threshold voltage of 1.75V and a series resistance of 3.5 ohms.

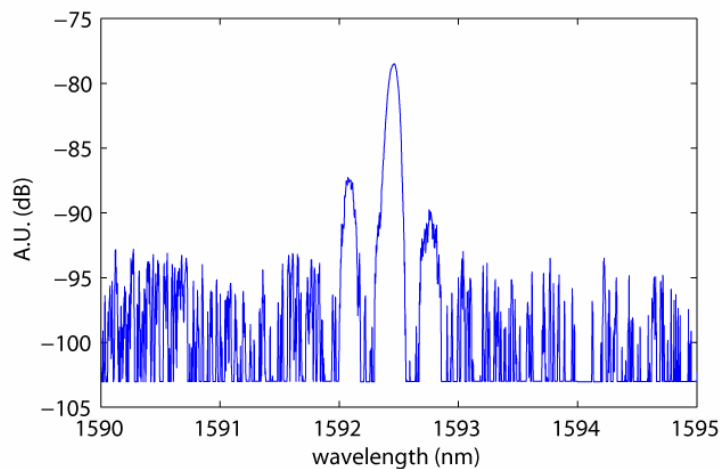


Fig. 6. The hybrid laser spectrum taken at 240mA for a $R = 100$, $L_{interaction} = 400$ microns

Figure 6 shows the measured multi-mode lasing spectrum of the laser driven at 240 mA. The spectrum was measured with an HP 70952A optical spectrum analyzer with a resolution bandwidth of 0.1 nm. The lasing wavelength is 1592.5 nm with a 0.21 nm mode spacing corresponding to a group index of 3.67.

Radius	$L_{\text{Interaction}}$	P_{max}	η_d	I_{th}	T_{max}
200 μm	600 μm	29 mW	13%	175 mA	60 C
	400 μm	27.5 mW	17%	175 mA	60 C
100 μm	300 μm	3.1 mW	12%	200 mA	65 C
	100 μm	7 mW	4.3%	150mA	65 C

Table 3: Max power, differential efficiencies, threshold currents and maximum operating temperatures

Table 3 shows the maximum output powers, differential efficiencies, threshold currents, and maximum output temperatures of the four device designs.

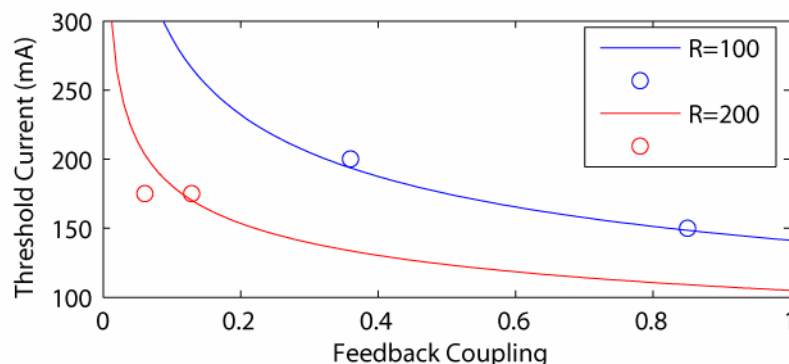


Figure 7: The experimental and fitted threshold currents

The experimentally fitted threshold currents are shown in Figure 7. The injection efficiency, modal loss, and g_0 were found to be 70%, 15 cm^{-1} , and 1500 cm^{-1} , respectively, in agreement with the hybrid silicon evanescent laser parameters reported in Ref. 18. The additional bend loss for 200 micron and 100 micron bends were found to be 0 cm^{-1} and 50 cm^{-1} , respectively. The discrepancy in the 50 cm^{-1} experimental bend loss and 22 cm^{-1} simulated bend loss for $R = 100$ micron data point is attributed to the steepness in that region of the simulated curve. Small deviations in the exact index values can cause significant changes in the simulated values.

Mode hopping between the degenerate clockwise and the counterclockwise propagating modes is traditionally a problem for ring lasers as it produces kinks in the single output L-I curves, see for example Figure 8a. This can be overcome and unidirectional lasing achieved by seeding one mode over the other with an external light source. We demonstrate an integrated version of this by forward biasing one of the photo-detectors to use as an amplified spontaneous emission (ASE) light source. Here the detector on the left of the laser (shown in Figure 2) is forward biased and used to seed the racetrack laser. Figure 8 shows the LI curve for the clockwise mode at three forward current levels on the left “detector” for the $R = 100$ micron, $L_{\text{interaction}} = 100$ micron device. It can be seen that at 50mA forward detector current, the output power is unstable due to mode hopping. At 75mA forward detector current, this LI becomes smoother, and at 100 mA, the clockwise propagating mode achieves stable lasing.

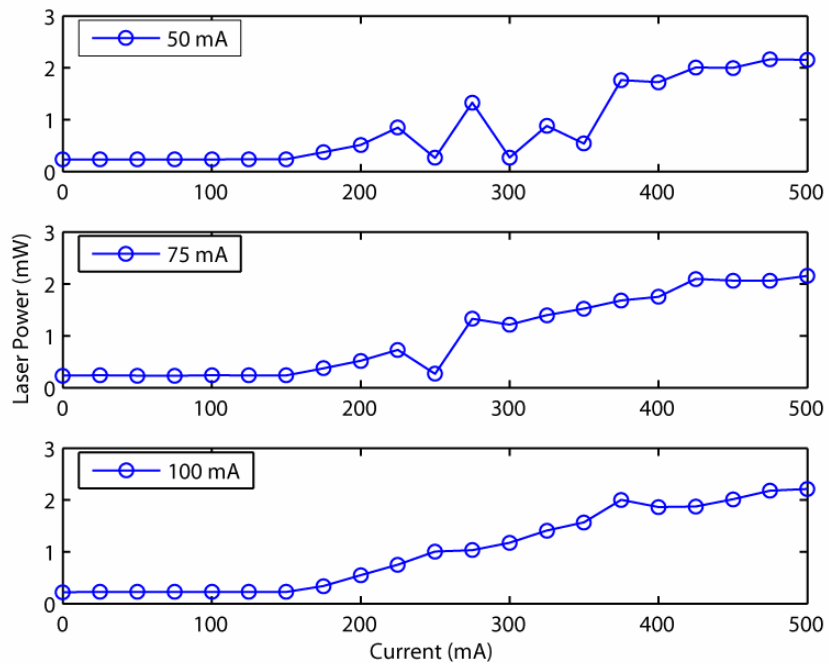


Fig. 8. The LI curve for the clockwise lasing mode for three forward bias currents for the photodiode on the left of a laser with $R = 100$ microns, and $L_{\text{interaction}} = 100$ microns.

5. Conclusion

The realization of a racetrack laser integrated with photodetectors illustrates the ability to create integrated photonic circuits using the hybrid silicon evanescent device platform. Moreover, on-chip testing and characterization of lasers eliminates the need for facet polishing and uncertainties cause by coupling losses and device dependencies on polishing quality. We have demonstrated a monolithic laser with output powers up to 29 mW operating up to 60 C in the range of 1590nm. The integrated photodetector shows a responsivity of ~ 1.11 A/W. Single wavelength lasing sources should be achievable by reducing the cavity length of these lasers to ~ 50 microns long or utilizing gratings to form DBR lasers.

Acknowledgments

The authors would like to thank K.-G. Gan, & B. R. Koch for insightful discussions and H.-H. Chang for help with device fabrication. We thank Intel & Jag Shah & Wayne Chang through DARPA for supporting this research through contracts W911NF-05-1-0175 and W911NF-04-9-0001.

References

1. G. T. Reed, "The optical age of silicon." *Nature* **427**, 615–618 (2004).
2. G. T. Reed, & A. P. Knights, *Silicon Photonics: An Introduction* (John Wiley, Chichester, West Sussex, 2004).
3. L. Pavesi, & D. J. Lockwood, *Silicon Photonics*, (Springer-Verlag, Berlin, 2004).
4. D. A. Miller, "Optical interconnects to silicon." *IEEE J. Sel. Top. Quant. Electron.* **6**, 1312–1317 (2000).
5. H. Rong *et al.* "A continuous-wave Raman silicon laser." *Nature* **433**, 725-728 (2005).
6. O. Boyraz, & B. Jalali, "Demonstration of a silicon Raman laser," *Opt. Express* **12**, 5269 (2004).
7. R. Espinola, J. Dadap, R. Osgood Jr., S. McNab, & Y. Vlasov, "Raman amplification in ultrasmall silicon-on-insulator wire waveguides." *Opt. Express* **12**, 3713-3718 (2004)
8. S. G. Cloutier, P. A. Kosyrev, & J. Xu, "Optical gain & stimulated emission in periodic nanopatterned crystalline silicon." *Nature Materials* **4**, 887, (2005).
9. P. Rojo Romeo, J. Van Campenhout, P. Regreny, A. Kazmierczak, C. Seassal, X. Letartre, G. Hollinger, D. Van Thourhout, R. Baets, J. M. Fedeli, and L. Di Cioccio, "Heterogeneous integration of electrically driven microdisk based laser sources for optical interconnects and photonic ICs", *Optics Express*, 14(9), p.3864-3871 (2006)

10. R. S. Jacobsen, *et al.*, "Strained silicon as a new electro-optic material," *Nature* **441**, 199-202 (2006)
11. A. Liu, L. Liao, D. Rubin, H. Nguyen, B. Ciftcioglu, Y. Chetrit, N. Izhaky, and M. Paniccia, "High-speed optical modulation based on carrier depletion in a silicon waveguide," *Opt. Express* **15**, 660-668 (2007)
12. V. R. Almeida, C. A. Barrios, R. R. Panepucci, M. Lipson, "All-optical control of light on a silicon chip," *Nature* **431**, 1081-1084 (2004)
13. L. Pavesi, L. Dal Negro, C. Mazzoleni, G. Franzò, & F. Priolo, "Optical gain in silicon nanocrystals," *Nature* **408**, 440-444 (2000).
14. A. Irrera, *et al.*, "Electroluminescence properties of light emitting devices based on silicon nanocrystals," *Physica E* **16**, 395-399 (2003).
15. B. Gelloz and N. Koshida, "Electroluminescence with high and stable quantum efficiency and low threshold voltage from anodically oxidized thin porous silicon diode," *J. Appl. Phys.* **88**, 4319-4324 (2000).
16. A. W. Fang, H. Park, O. Cohen, R. Jones, M. J. Paniccia, and J. E. Bowers, "Electrically pumped hybrid AlGaInAs-silicon evanescent laser," *Opt. Express* **14**, 9203-9210 (2006)
17. A. W. Fang, R. Jones, H. Park, O. Cohen, O. Raday, M. J. Paniccia, and J. E. Bowers, "Integrated AlGaInAs-silicon evanescent race track laser and photodetector," *Opt. Express* **15**, 2315-2322 (2007)
18. H. Park, A. W. Fang, R. Jones, O. Cohen, M. J. Paniccia, and J. E. Bowers, "40 C Continuous-Wave Electrically Pumped Hybrid Silicon Evanescent Laser," International Semiconductor Laser Conference 2006 (ISLC 2006), post deadline paper, September 2006
19. D. Pasquariello, *et al.* "Plasma-Assisted InP-to-Si Low Temperature Wafer Bonding," *IEEE J. Sel. Top. Quantum Electron.* **8**, 118, (2002).
20. H. Boudinov, H. H. Tan, & C. Jagadish., "Electrical isolation of n-type and p-type InP layers by proton bombardment," *J. Appl. Phys.* **89-10**, pp. 5343-5347, (2001)